Transactions on Computer Science and Intelligent Systems Research
ISSN: 2960-1800, eISSN: 2960-2238 | Volume 11
TPCEE 2025

The Architecture of Resonance: Decoding How an Acoustic Cavity Shapes Sound Pressure Levels

Qiyuan Xi

The High School Affiliated to Beijing Normal University, Beijing, China

clx328588@qq.com

Abstract. This study investigates the acoustic performance of microspeakers across various cavity configurations using coupled electromagnetic-mechanical-acoustic (E-M-A) simulations and experimental validation. A modular test setup was developed to accommodate interchangeable microspeaker modules with distinct cavity designs, including front-firing, side-firing, and back cavity geometries. The results demonstrate that side-firing cavities induce a distinct Helmholtz resonance peak in the mid-frequency range, while the back cavity contributes additional acoustic compliance, effectively shifting the system's resonant frequency. Experimental measurements show strong agreement with simulation results, confirming the effectiveness of the coupled E-M-A method for optimizing microspeaker-cavity systems to achieve desired frequency responses.

Keywords: Electroacoustic; Multi-physics coupling; Acoustic cavity; Sound pressure level.

1. Introduction

The rapid expansion of consumer electronics and the IoT ecosystem has created a strong demand for compact, high-performance audio components. Microspeakers [1], essential in devices such as smartphones, laptops, and smart sensors, face increasing pressure to deliver high-fidelity sound within increasingly thin form factors. While intrinsic factors—magnetic circuit, voice coil, and diaphragm—determine baseline performance, the external acoustic environment formed by device cavities plays an equally critical role.

In real-world devices, microspeakers operate within front, back, and often side-firing cavities, each of which alters acoustic loading and affects frequency response [2], THD, and especially resonant frequency. However, traditional reliance on iterative prototyping limits efficiency, and existing studies lack a systematic, predictive understanding of how specific cavity configurations influence acoustic output.

To resolve this, the present study utilizes a multi-physics coupling simulation approach [3] to analyze micro speaker behavior under controlled cavity designs. An integrated framework combining structural design, high-fidelity simulation, and experimental validation was developed, including modular test fixtures with interchangeable cavities. Using an E-M-A coupling method [4, 5], this work clarifies the distinct acoustic roles of each cavity: the side-firing cavity produces a characteristic mid-frequency peak via Helmholtz resonance, while the back cavity adds mechanical stiffness, shifting the system's resonant frequency downward.

2. Analysis method

2.1. Electromagnetic Force Generation

The force generation in a voice coil system is primarily governed by electromagnetic principles, which can be categorized into magnetic attraction force and electromagnetic force.

1) Magnetic Attraction Force This force occurs from the interaction between ferromagnetic materials and permanent magnets, even without an electric current.

2) Electromagnetic Force When the headphone's circuit system is energized, two main electromagnetic phenomena occur:

- Solenoid Force: Generated due to the current-carrying coil acting as an electromagnet.
- Lorentz Force: Produced when the current interacts with the magnetic field in the air gap.

The resultant electromagnetic force can be expressed using the Lorentz force Equation 1:

$$Fem=i(t)\cdot L\times B \tag{1}$$

Where, B is the magnetic flux density in the air gap (Tesla), L is the effective length of the voice coil wire (m), and $i(t)$ is the time-varying current (A).

The core of the headphone driver unit lies in the voice coil-magnetic circuit system, where the electromagnetic force can be described using Maxwell's stress tensor. The magnetic flux density B follows the magnetostatic governing Equation 2 and 3:

$$\nabla\times H=J \tag{2}$$

$$B=\mu_0\mu_r H \tag{3}$$

Where, J is the current density in the voice coil, and μ_r is the relative permeability of the material.

The Lorentz force density acting on the voice coil in the magnetic field is given by: $fv=J\times B$. For an N-turn voice coil, the total magnetic force can be obtained by integrating the Maxwell stress tensor over the surface: $F=\oint T_{ij}n_i dS$ Here, T_{ij} (Equation 4) represents the Maxwell stress tensor, which describes both electrostatic and magnetostatic forces:

$$T_{ij}=\epsilon 0(EiEj-\frac{1}{2}\delta ijE^2)+\frac{1}{\mu 0}(BiBj-\frac{1}{2}\delta ijB^2) \tag{4}$$

In headphone drivers, the magnetic field distribution is typically axisymmetric, allowing the driving force Equation 5 to be simplified as:

$$F_{em}=\frac{B^2A}{2\mu_0}\cdot\frac{dl}{dx} \tag{5}$$

Where, A is the cross-sectional area of the magnetic gap, L is the equivalent inductance of the magnetic circuit, and x is the displacement of the voice coil.

2.2. Mechanical Vibration Model

The elastic properties of solid vibrations are characterized by the stiffness coefficient k (unit: N/m), which fundamentally represents a material's resistance to deformation. According to Hooke's Law, the restoring force F_k of a spring is proportional to the displacement x and acts in the opposite direction, as shown in Equation 6:

$$F_k=-kx \tag{6}$$

The mass m (unit: kg) represents the inertial effect of the system, following Newton's Second Law, as shown in Equation 7:

$$F_m=ma=m\frac{d^2x}{dt^2} \tag{7}$$

In vibration systems, the acceleration of the mass opposes the displacement direction. Combining this with Hooke's Law, the undamped free vibration Equation becomes Equation 8:

$$m\frac{d^2x}{dt^2}+kx=0 \tag{8}$$

The solution to this Equation is simple harmonic motion, as shown in Equation 9:

$$x(t)=A\cos(\omega_n t+\phi) \tag{9}$$

Where the natural angular frequency is Equation 10:

$$\omega_n=\sqrt{k/m} \tag{10}$$

Real-world solid vibrations involve energy dissipation due to factors such as internal material friction and air resistance. The damping force F_c is typically proportional to velocity (viscous damping model), as shown in Equation 11:

$$F_c=-c\frac{dx}{dt} \tag{11}$$

Here, c is the damping coefficient (unit: N·s/m), and the negative sign indicates that the damping force opposes the motion direction. The complete damped dynamic Equation 12 is:

$$m\frac{d^2x}{dt^2}+c\frac{dx}{dt}+kx=0 \tag{12}$$

2.3. Acoustic Cavity Modeling

The headphone cavity acts as a Helmholtz resonator whose resonance frequency is given by:

$$f_{res}=\frac{c_0}{2\pi}\sqrt{\frac{S}{VL_{eff}}} \tag{13}$$

Where $L_{eff}=L+0.85\sqrt{S}$ is the effective length. The system exhibits two resonance peaks: 1. low-frequency (100-1000Hz); 2. high-frequency range.

Acoustic cavities play a key role in microspeaker design, shaping both frequency response and sound field performance. Common cavity models include an open-ended tube, a closed cavity, and a Helmholtz resonator (HR) [6], as shown in Figure 1. These models treat the cavities as lumped elements for coupling with diaphragm dynamics.

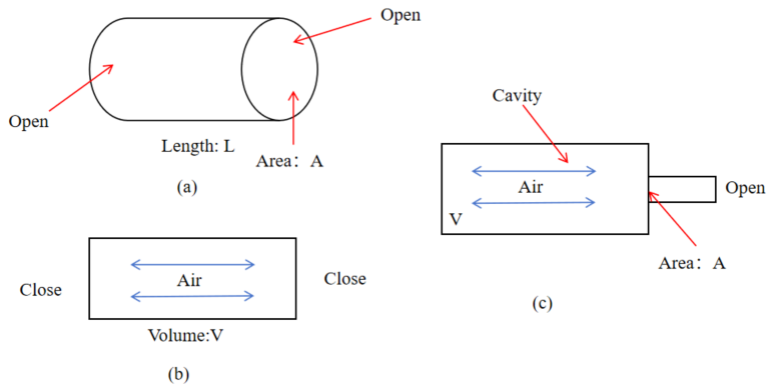

Figure 1. (a) tube with two open ends; (b)closed cavity; and (c) Helmholtz resonator

1) A tube open at both ends with rigid walls behaves as an acoustic mass if it is sufficiently short such that the air inside it moves without appreciable compression. The acoustic mass M_{ac} of the two open-end tubes is given by Equation 14.

$$M_{ac}=\frac{\rho L}{A}\ [\mathrm{kg}/m^4] \tag{14}$$

Where ρ, L, and A denote air density, tube length, and cross-sectional area, respectively.

2) In the low-frequency limit, an applied external pressure compresses the enclosed air in the cavity, which then acts as a spring because of elasticity [7]. The acoustic spring constant of the closed cavity K_{ac} is given by Equation 15.

$$K_{ac}=\frac{\rho c^2}{V}\ [\mathrm{N}/m^5], \tag{15}$$

The direct analogy relationship between acoustic and mechanical analyses is shown in Equation 16.

$$M_{me}=M_{ac}A^2\ ,\ K_{me}=K_{ac}A^2 \tag{16}$$

Where V, M_{me}, and K_{me} denote cavity volume, lumped mechanical mass, and lumped mechanical stiffness, respectively.

3) The Helmholtz resonator can be treated as a mechanical mass-spring system with a natural frequency f_{HR}. c is the air speed.

$$f_{HR}=\frac{1}{2\pi}\sqrt{\frac{K_{me}}{M_{me}}}=\frac{1}{2\pi}\sqrt{\frac{A^2\rho_0 c^2}{\rho_0 LAV}}=\frac{c}{2\pi}\sqrt{\frac{A}{LV}} \tag{17}$$

In acoustics, end correction is a short distance applied or added to the actual length of a resonance tube to calculate the precise resonant frequency.

Hydraulic diameter [8] allows flow analysis in non-circular channels similarly to circular tubes. For a rectangular cross section with width b and height a, the hydraulic diameter is given by Equation 18.

$$D_{\mathrm{h}}=\frac{2ab}{a+b},\ b\gg a, \tag{18}$$

The Helmholtz resonator considering an end correction (HREC) is given by Equation 19.

$$f_{HREC}=\frac{c}{2\pi}\sqrt{\frac{A}{(L+0.85D_h)V}}, \tag{19}$$

2.4. Multiphysics E-M-A Coupling

The E-M-A coupling method of the microspeaker [9, 10] uses the coupled Equations of the voltage, mechanical vibration, and acoustic wave Equations, which are shown in Equations 20~22, respectively.

$$V_e=iR_e+L_e\frac{di}{dt}+K_fv \tag{20}$$

Where V_e, i, R_e, K_f, and v are the input voltage, electrical current, direct current resistance of the voice coil, inductance, force factor, and mechanical velocity, respectively.

$$[M]\{a\}+[R]\{v\}+[K]\{z\}=\{F_L\}+\{F_P\} \tag{21}$$

Where [M], {a}, [R], {v}, [K], {z}, $\{F_L\}$, and $\{F_P\}$ are the mass, acceleration, damping, velocity, stiffness, displacement, Lorentz force, and pressure force vectors, respectively.

$$\nabla^2P+k^2P=0, \tag{22}$$

Where ∇^2, P, and k are the Laplace operator, acoustic pressure, and wavenumber, respectively.

Equations 23~26 indicate the coupled relationships between the electromagnetic, mechanical, and acoustic domains.

$$V_{Backemf}=K_f\dot{z}, \tag{23}$$

$$F_L=K_fI \tag{24}$$

$$F_P=S_dP \tag{25}$$

$$U=S_dv, \tag{26}$$

Where $V_{Backemf}$, S_d, and U represent the back electromotive force, effective radiation area, and volume velocity, respectively. The E-M-A coupling model is illustrated in Figure 2.

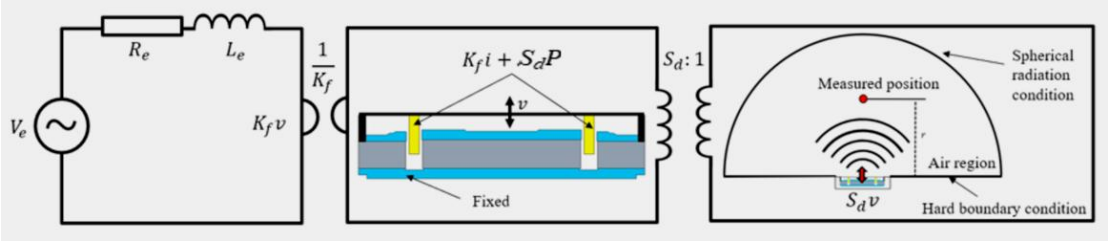

Figure 2. Electromagnetic-mechanical-acoustic coupling model

3. Experiments

3.1. Experimental setup

The experimental setup comprises a 1 m³ square anechoic chamber lined with 5 mm acoustic foam to minimize external noise (Figure 3). A DG1022 digital oscilloscope generates sinusoidal signals (0–20 V) for the speaker (Figure 4a), while a DT8852 SPL meter records sound pressure levels from 100–8000 Hz (Figure 4b). Tests are conducted on a computer with an Intel Core i9-13980HX CPU and 16 GB RAM.

Figure 3. Square anechoic chamber: (a) outer structure; and (b) inner structure.

Figure 4. Experimental setup: (a) digital oscilloscope; and (b) sound pressure level meter

The experimental setup, shown schematically and physically in Figure 5, places the SPK module and SPL meter inside an anechoic chamber. The SPK is driven by a digital oscilloscope via signal cables, while the SPL meter connects to a computer for synchronized data acquisition. Sinusoidal signals were applied from 200–4000 Hz in 100 Hz steps.

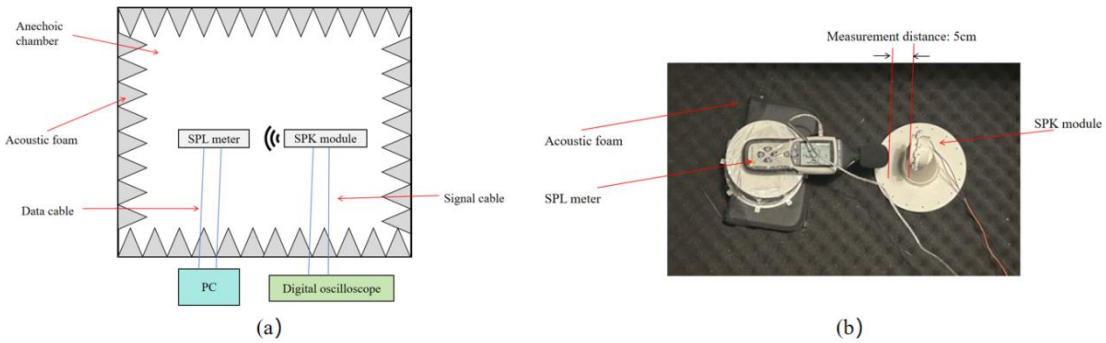

Figure 5. Experimental condition: (a) schematic diagram; and (b) physical photograph

3.2. Experimental samples

The experimental sample includes a speaker (4 Ω, 3 V, 0.6 N/A) and a 3D-printed acoustic cavity. The SPK module, with front/back cavities, voice coil, diaphragm, and magnetic circuit, is shown in

Figure 6, and photos of the speaker with three cavity designs—front-, side-, and combined-firing—are in Figure 7.

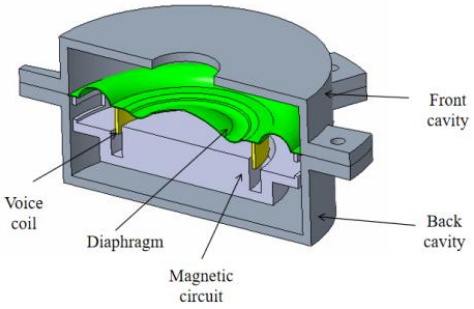

Figure 6. The 3D modeling of SPK module

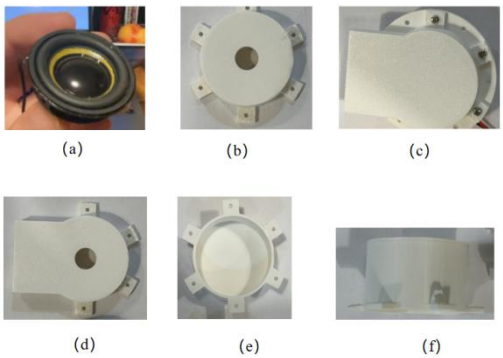

Figure 7. Physical photograph of the SPK module: (a) SPK unit; (b) front-firing cavity; (c) side-firing cavity; (d) combined-firing cavity; (e) back cavity(top view); and (f) back cavity (side view)

Tests were conducted for different acoustic cavity configurations (Table 1). Group 2 has a back cavity volume twice that of Group 1, while Groups 3 and 4 have front cavity volumes double those of Groups 1 and 2, respectively. H1 and H2 denote the heights of the front and back cavities.

Table 1. SPK unit with different cavity designs

Group	Name	H1 (mm)	Sound outlet type	H2 (mm)
Group 1	Type 1-1	12.5	Front-firing	20.0
	Type 1-2		Side-firing	
	Type 1-3		Combined-firing	
Group 2	Type 2-1	12.5	Front-firing	40.0
	Type 2-2		Side-firing	
	Type 2-3		Combined-firing	
Group 3	Type 3-1	25.0	Front-firing	20.0
	Type 3-2		Side-firing	
	Type 3-3		Combined-firing	
Group 4	Type 4-1	25.0	Front-firing	40.0
	Type 4-2		Side-firing	
	Type 4-3		Combined-firing	

The real sample of type 1 with different views are shown in Figure 8. The top view of Group 1's samples are shown in Figure 9. The SPL meter is set in different positions due to the outlet cavities, the measurement distance is the same as 5cm away from the acoustic outlet, the measurement position of combined-firing is the same as side-firing cavity.

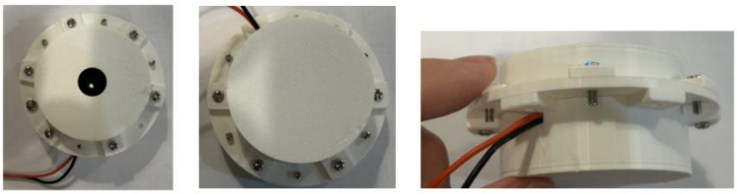

Figure 8. Type 1-1 sample: (a) top view; (b) bottom view; and (c) side view

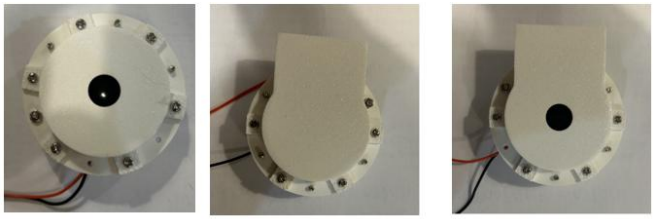

Figure 9. Group 1: (a) Type 1-1; (b) Type 1-2; and (c) Type 1-3

3.3. Experiment Procedures

Step 1: Speaker Module Assembly

According to the Table 1, the different back cavity of SPK modules are shown in Figure 10, including type 1-2, and type 2-2.

Figure 10. Different back cavity SPK modules: (a) type 1-2; and (b) type 2-2

Step 2: Data Acquisition

After assembling the SPK module, the SPL meter was positioned near the sound outlet and connected to the computer. The digital oscilloscope was initiated via software, with driving frequencies starting at 200 Hz and increasing in 100 Hz steps. At each frequency, the system was allowed to stabilize before recording the driving frequency and corresponding SPL.

Step 3: Data Analysis

Frequency and weighted SPL data were correlated for each cavity configuration, with SPL plotted against frequency. The SPL meter was kept at a constant distance, and each group was tested twice to reduce error. Measured SPL curves were then compared with theoretical acoustic models.

4. Results and discussion

4.1. Simulation setting

COMSOL Multiphysics was used for E-M-A coupling analysis, with the air domain modeled as an anechoic chamber (no incoming acoustic waves). The SPK module was centered in the air domain, with the measurement position matching the experimental setup. Physics domain settings and FEM modeling are shown in Figure 11.

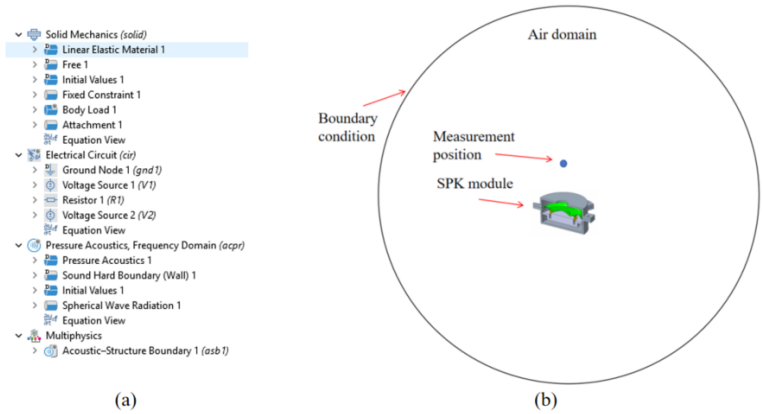

Figure 11. The simulation modeling: (a) domain setting; and (b) FEM modeling

4.2. Results comparison

4.2.1. Group 1 result comparison.

Experimental results for Group 1 are shown in Figure 12(a). Type 1-3 exhibits lower SPL than types 1-1 and 1-2 at 200–1000 Hz due to dual acoustic outlets. SPL reductions from 1260–4000 Hz are attributed to the woofer-type SPK unit. Types 1-2 and 1-3 show a 3150 Hz peak from Helmholtz resonance, with side-firing pressure distribution in Figure 13. SPL comparisons between experiment and simulation show good agreement, especially at high-frequency peaks (Figure 12a–c), with minor differences from room noise. Acoustic pressure distributions at 1260 Hz differ significantly among the three outlet types (Figure 14).

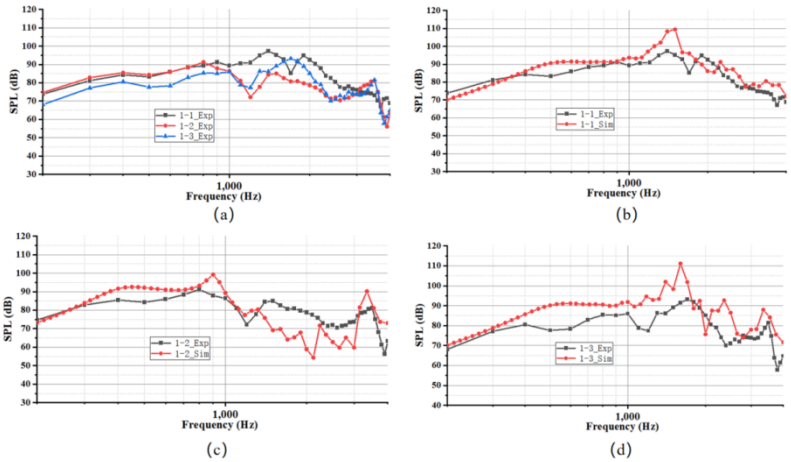

Figure 12. SPL result of Group 1: (a) different types; (b) type 1-1; (c) type 1-2; and (d) type 1-3

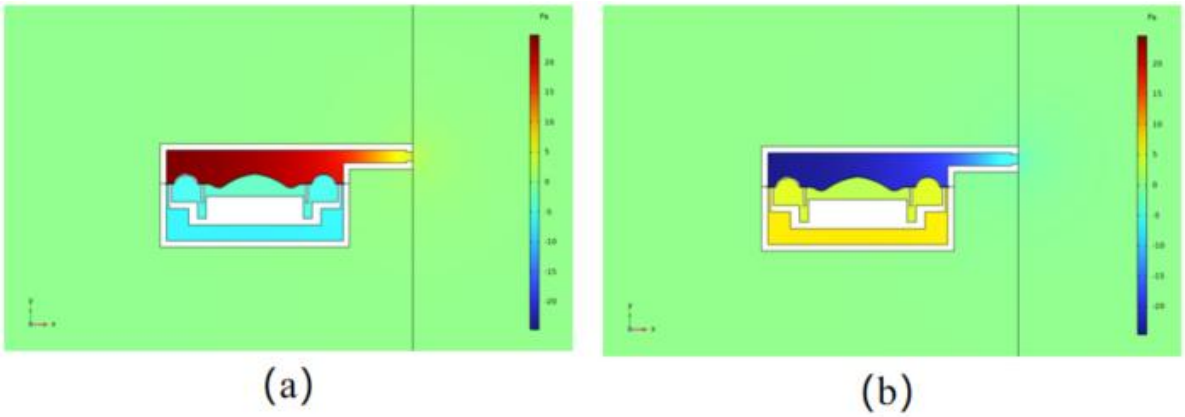

Figure 13. The acoustic pressure distribution of type 1-3 at 3150Hz: (a) in-phase; and (b) out of phase

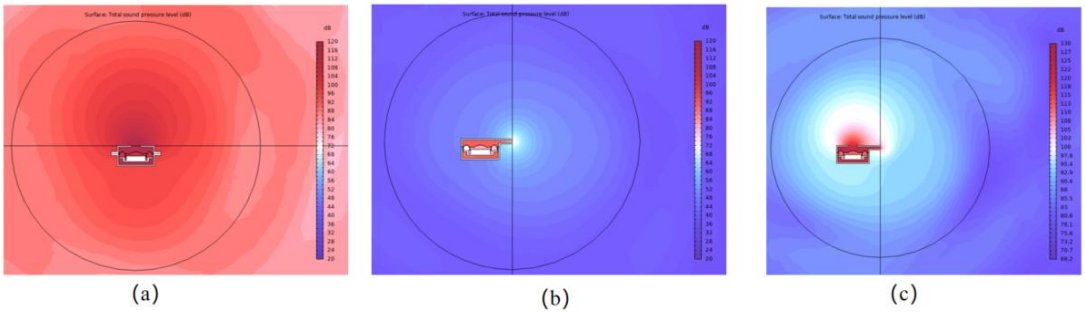

Figure 14. The acoustic pressure distribution at 1260Hz (a) type 1-1; (b) type 1-2; and (c) type 1-3

4.2.2. Group 2 result comparison.

Experimental results for Group 2, which has a larger back cavity than Group 1, are shown in Figure 15(a). SPL comparisons for types 2-1, 2-2, and 2-3 show good agreement between experiment and simulation (Figure 15a–c). Acoustic pressure distributions at 1260 Hz differ notably (Figure 16). Simulation comparisons between types 1-2 and 2-2 indicate that the larger back cavity lowers the mechanical resonant frequency, while Helmholtz resonance remains unchanged due to identical side-firing cavities (Figure 17).

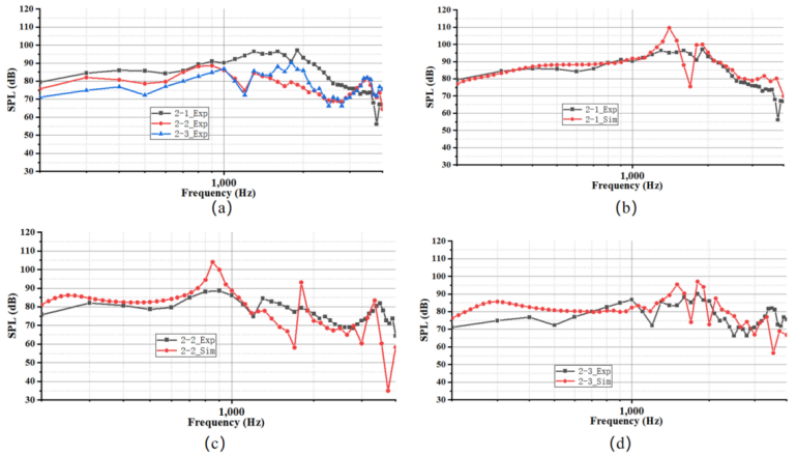

Figure 15. SPL result of Group 2: (a) different types; (b) type 2-1; (c) type 2-2; and (d) type 2-3

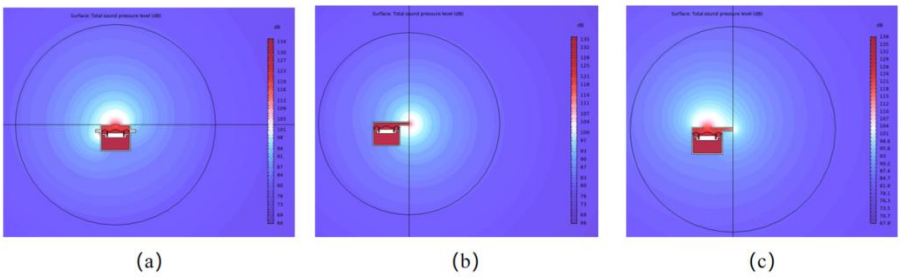

Figure 16. The acoustic pressure distribution at 1260Hz (a) type 2-1; (b) type 2-2; and (c) type 2-3

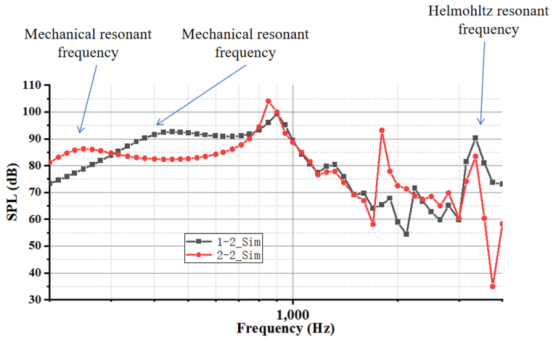

Figure 17. Type 1-2 Vs Type 2-2

4.2.3. Group 3 result comparison.

Experimental results for Group 3 are shown in Figure 18(a), with SPL comparisons for types 3-1, 3-2, and 3-3 demonstrating good agreement between experiment and simulation (Figure 18a–c). Acoustic pressure distributions at 1260 Hz differ notably (Figure 19). Simulation comparisons between types 1-2 and 3-2 show identical mechanical resonance but differing Helmholtz resonance due to side-firing cavity size, with larger cavities yielding lower resonance frequencies.

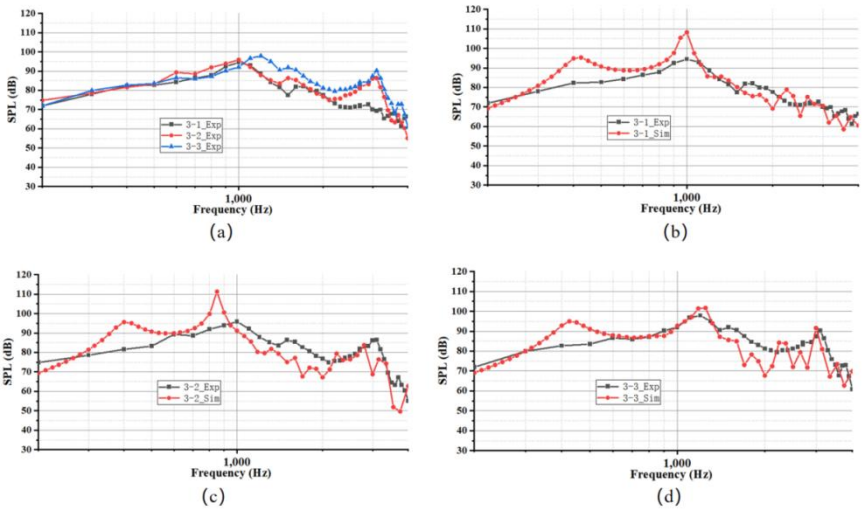

Figure 18. SPL result of Group 3: (a) different type; (b) type 3-1; (c) type 3-2; and (d) type 3-3

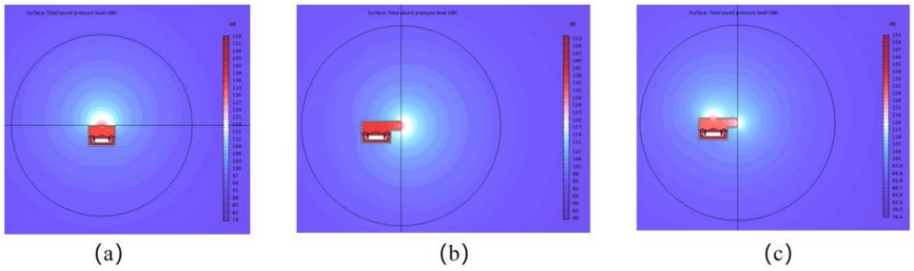

Figure 19. The acoustic pressure distribution at 1260Hz (a) type 3-1; (b) type 3-2; and (c) type 3-3

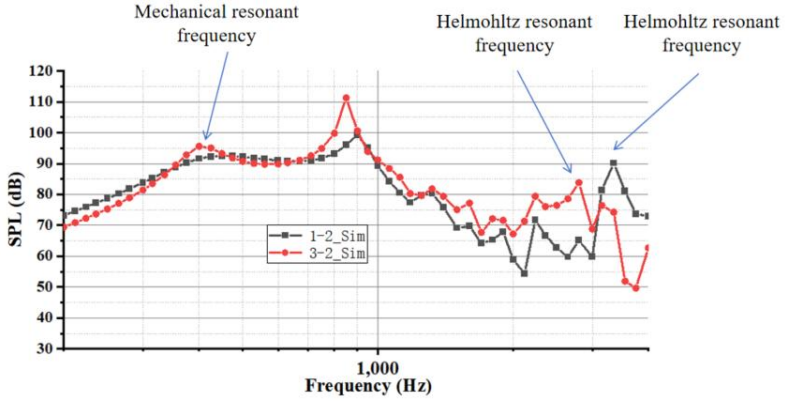

Figure 20. Type 1-2 Vs Type 3-2

4.2.4. Group 4 result comparison.

Experimental results for Group 1 are shown in Figure 19(a), with SPL comparisons for types 4-1, 4-2, and 4-3 demonstrating good agreement between experiment and simulation (Figure 19a–c). Acoustic pressure distributions of Group 4 at 1260 Hz differ significantly (Figure 20). Simulation comparisons between types 1-2 and 4-2 (Figure 21) reveal that variations in back cavity volume shift the mechanical resonance, while differences in side-firing cavity size affect Helmholtz resonance, with larger cavities yielding lower resonance frequencies.

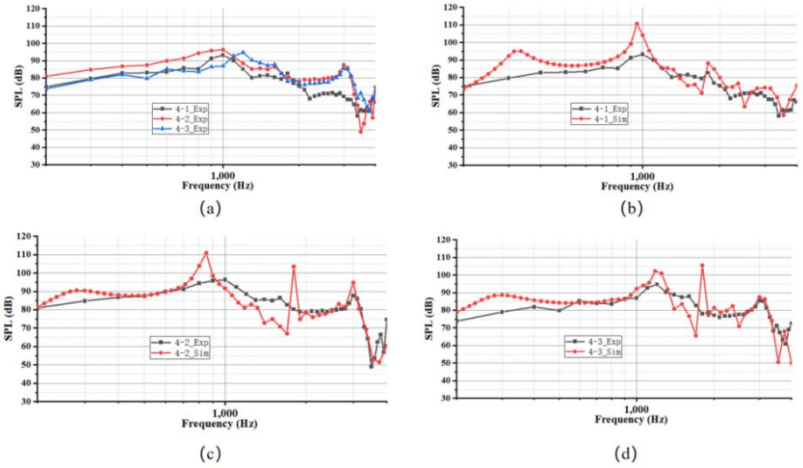

Figure 21. SPL result of Group 4: (a) different type; (b) type 4-1; (c) type 4-2; and (d) type 4-3

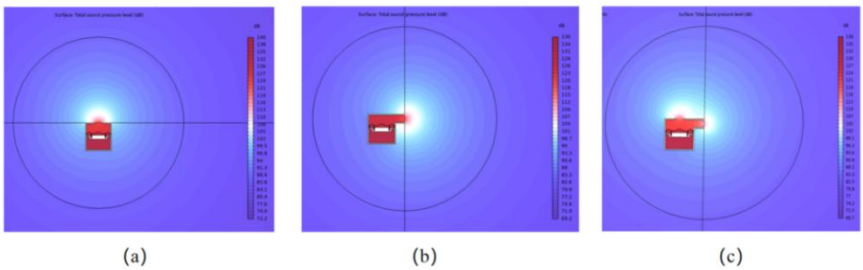

Figure 22. The acoustic pressure distribution at 1260Hz (a) type 4-1; (b) type 4-2; and (c) type 4-3.

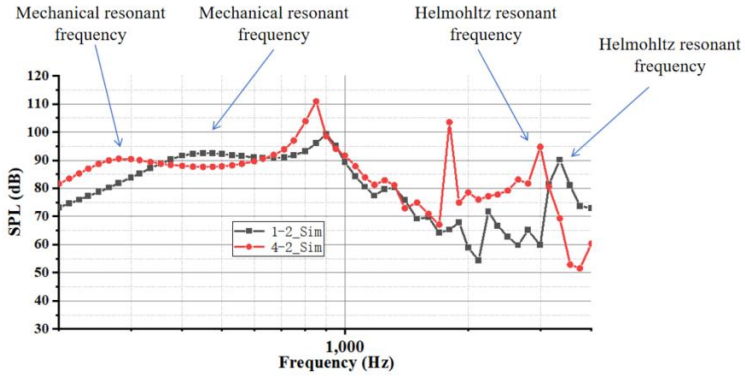

Figure 23. Type 1-2 Vs Type 4-2

5. Conclusion

This study investigated the impact of acoustic cavity designs on microspeaker performance using combined multi-physics simulation and experimental validation. E-M-A coupling accurately captured multi-domain behavior, showing strong agreement with measurements. Results indicate that back cavity volume mainly affects mechanical resonance, side-firing geometry governs Helmholtz resonance, and combined-firing designs produce interference that reduces SPL at specific frequencies. The findings demonstrate the effectiveness of E-M-A coupling for microspeaker design, offering guidance for compact acoustic devices and reducing reliance on physical prototyping. Future work will examine more complex cavity geometries and wider frequency ranges.

Acknowledgements

First and foremost, I would like to express my sincere gratitude to my advisor, Mr. Gao Yisai, a physics teacher at Beijing Normal University Experimental High School, for his invaluable guidance throughout this research. From literature recommendations to experimental design and theoretical

modeling, his support was crucial to the success of this project. His mentorship allowed me to gain proficiency in software tools such as MATLAB, COMSOL, and SolidWorks, enabling me to effectively cross-validate data through simulations and physical experiments.

I would also like to thank the school teachers for their support with equipment and the students who assisted with data recording. Lastly, I declare that all guidance provided by Mr. Gao was purely academic and uncompensated.

References

[1] Jiang, Z. X., Xu, D. P., Park, K. T., & Hwang, S. M. (2024). Design and analysis of two-way microspeaker to enhance mid-frequency sound pressure level. Sensors and Actuators A: Physical, 365, 114914.

[2] Lin, C. H., Tseng, C., Lo, S. C., Lai, M. F., & Fang, W. (2025, June). SPL and THD Improvement of Piezoelectric MEMS Microspeaker via Parallel Dual Curve Springs with Ring Actuator. In 2025 23rd International Conference on Solid-State Sensors, Actuators and Microsystems (Transducers) (pp. 451-454). IEEE.

[3] Kitamura, K., & Kajikawa, Y. (2022, October). A New Analysis Method for Frequency Response Analysis of Micro-speaker Using Equivalent Circuit and Finite Element Method. In 2022 IEEE 11th Global Conference on Consumer Electronics (GCCE) (pp. 597-598). IEEE.

[4] Park, K., Jiang, Z., Oh, Y., & Hwang, S. (2024, June). Novel Microspeaker Design for Smartwatches with Integrated Woofer and Tweeter Units. In 2024 IEEE 21st Biennial Conference on Electromagnetic Field Computation (CEFC) (pp. 1-2). IEEE.

[5] Bai, M. R., You, B. C., & Lo, Y. Y. (2014). Electroacoustic analysis, design, and implementation of a small balanced armature speaker. The Journal of the Acoustical Society of America, 136 (5), 2554-2560.

[6] Selamet, A., & Lee, I. (2003). Helmholtz resonator with extended neck. The Journal of the Acoustical Society of America, 113 (4), 1975-1985.

[7] Sun, P., Xu, D. P., & Hwang, S. M. (2014). Design of microspeaker module considering added stiffness. Journal of Mechanical Science and Technology, 28 (5), 1623-1628.

[8] Al_Omari, A. K., Saied, H. F. I., & Avrunin, O. G. (2011). Analysis of changes of the hydraulic diameter and determination of the air flow modes in the nasal cavity. In Image Processing and Communications Challenges 3 (pp. 303-310). Berlin, Heidelberg: Springer Berlin Heidelberg.

[9] “Impedance Spectroscopy: Theory, Experiment, and Applications” (Barsoukov & Macdonald).

[10] “Electrochemical Impedance Spectroscopy” (Orazem & Tribollet).